NASA Technical Memorandum 102200

Calibration of Seven-Hole Pressure Probes for Use in Fluid Flows with Large Angularity

Gregory G. Zilliac
Ames Research Center, Moffett Field, California

December 1989

National Aeronautics and
Space Administration

Ames Research Center
Moffett Field, California 94035

SYMBOLS

C_P	pressure coefficient, $C_P = (P - P_\infty)/(1/2\rho U_0^2)$
$C_{P_{i,...}}$	multihole probe pressure coefficients
c	A-D counts
e	a measurement-system dependent quanitity
F	equation of probe surface
h	manometer height
P	pressure
r, θ, z	probe-cylindrical coordinate directions
R	distance to probe surface in r-direction, or a result of a measurement
u, v, w	velocity components in x, y, z-directions
U	freestream velocity
x, y, z	right-hand Cartesian coordinate directions
α	multihole probe angle of attack
β	sideslip angle for multihole probe
γ	cocked-probe stem angle
ς	angle between x-axis and freestream flow direction
η	circumferential pressure tap location
θ	pitch angle for multihole probe
ν	air kinematic viscosity
ξ	transformed circumferential coordinate
ρ	air density
Φ	velocity potential
χ	angle of rotation
ψ	yaw angle for multihole probe

Subscripts

d	probe or cylinder diameter
m	manometer
n	pressure probe hole or sector number
ref	reference value
z	zero applied pressure difference
$total$	freestream total pressure
$static$	freestream static pressure
∞	refers to freestream conditions

1. SUMMARY

This report describes the calibration of a non-nulling, conical, seven-hole pressure probe over a large range of flow onset angles. The calibration procedure is based on the use of differential pressures to determine the three components of velocity. The method allows determination of the flow angle to within 0.5° and velocity magnitude to approximately 1.0%. Also included is an examination of the factors which limit the use of the probe, a description of the measurement chain, an error analysis, and a typical experimental result. In addition, a new general analytical model of pressure probe behavior is described and the validity of the model is demonstrated by comparing it with experimentally measured calibration data for a three-hole yaw meter and a seven-hole probe.

2. INTRODUCTION

Multihole pressure probes have long been used to obtain velocity and pressure information in fluid flows. A multitude of probe geometries have been developed, including certain probes which are highly application-specific (e.g., turbomachinery, boundary layers, and free shear flows). Reference 1 presents a concise summary of the different types of probes and their calibration. The basic principle of operation, which most multihole probes have in common, is the ability to determine velocity magnitude and direction from a measured pressure differential. The particular choice of a probe type depends on interference effects, probe access, probe volume, time response to mean pressure changes, sensitivity, and flow inclination to the probe, among others.

The seven-hole probe was designed only recently for flows where the angle of the velocity vector can be large with respect to the probe axis. It is possible to get comparable accuracy using a four- or five-hole probe in a nulling mode, but nulling a probe can often be difficult, especially near the surface of a body. In addition, because of the convenient fact that six tubes of equal diameter fit exactly around a single tube of the same diameter, there is only a minimal advantage to using fewer than seven holes as far as probe volume is concerned. Development of the probe and calibration technique is described in reference 2. Further refinements of the same basic technique are presented in references 3,4, and 5. Contained in this report is a thorough examination of seven-hole probe calibration theory and the factors which govern the use of seven-hole probes.

The seven-hole probe calibration technique described in reference 2 involves positioning the probe at known angles to the flow and then measuring the seven pressures. Dimensionless velocity-invariant pressure coefficients, based on combinations of differences between the

seven measured pressures, are formed. Third-order polynomial functions for the flow properties are then determined based on the pressure coefficients and the known probe inclination. Upon using the probe in an unknown flow field, a sectoring scheme is used to choose certain combinations of the pressure coefficients depending on the relative magnitudes of the seven measured pressures. This sectoring approach, which is the essence of the seven-hole probe technique, permits measurement in flows of high angularity by selecting pressure probe holes which have the greatest sensitivity to the flow (i.e., holes for which the flow on the probe remains attached) being measured.

The calibration approach developed by Gallington is unique, and in many ways, quite ingenious. It is flexible and can be applied to any seven-hole probe configuration. The principles on which the calibration is based, are physical principles (nonempirical) which can be analytically modelled. With careful application of the calibration techniques, a high degree of accuracy can be achieved.

In the present effort, a few improvements have been made in order to simplify the calibration process and increase the accuracy. As shown in reference 5, the polynomial expressions used to determine the flow onset angle (based on approximately 20 calibration points, and a 5° increment between points) can have a substantial standard deviation (deviation of the curve-fit from the actual data at the basepoints of the data) of up to 1.4°. To reduce these errors, the approach taken herein is to use interpolation of the calibration data rather than curve-fitted polynomial expressions. A drawback of this approach is that there are no response equations which cover the entire range of the probe.

Another difficulty, which is identified in reference 2, is that a method needs to be developed to determine if the flow on the probe is separated to such a degree to render the probe unuseable. If a data point is taken in a flow where the flow angle exceeds the maximum allowable for the probe, the data point may interpreted to be within the flow angle range of the probe. This situation is, at times, difficult to detect and can lead to serious measurement errors. The present calibration technique includes a check on the validity of a measured point to indicate whether the flow angle is out of bounds.

When a probe is being selected or designed for a specific application, because of the large number of possible configurations, choices are often made based on minimal performance information, rules of thumb, and experience. An accurate, easy-to-use method of determining specific information such as probe sensitivity is desirable, especially during the probe design phase. Existing analytical methods in the literature can be classified as either being based on slender-body theory or based on potential flow-singularity methods. Reference 6 presents the pros and cons of the two approaches. The main arguments in favor of the slender-body approach is that it is possible to derive explicit analytic expressions for the calibration functions. These expressions allow one to gain insight into the various scaling laws which govern probe behavior. Unfortunately, the accuracy of the slender-body technique is limited by the slender-body assumption. The main advantage of the singularity method approach

is that an accurate numerical solution may be computed for complicated probe geometries. The penalty is the amount of computer time required for one solution of a typical panel method. The conclusion of this reference is that slender body theory is preferred with the recognition that all analytical methods are too approximate to preclude calibration.

Both methods have been investigated in the present study and, as will be shown, the slender body approach was found to be too inaccurate to give much useful information to probe designers. As a result, an efficient analytical method has been developed, based on a novel use of a panel method, to give a relatively accurate prediction of probe behavior.

The main objective of this report is to look at the theory of multihole probe operation and show how this theory applies to seven-hole probes. A secondary objective is to demonstrate a model of probe behavior which can be used to design a probe that is tailored to specific applications. Additionally, this report documents a seven-hole probe calibration procedure, which has been developed and used in a study of the flow past a body of revolution at a high angle of attack.

3. MULTIHOLE PROBE THEORY

This section contains the fundamentals of multihole probe theory. Included is a discussion of the pressure coefficient normalization, an outline of the seven-hole probe calibration procedure, a sample result, a description of a general pressure probe analytical model, and an error analysis.

3.1 Pressure Coefficient Normalization

Prior to the description of the seven-hole probe calibration technique, it is necessary to detail how typical multihole probe calibration schemes work. In general, as can be deduced from the descriptions of several different multihole calibration procedures presented in reference 1, there are features which most schemes have in common. The salient feature is a normalization procedure which, when applied to the pressure differences measured between two taps on the face of a multihole probe, allows the formulation of pressure coefficients which are dependent on flow direction and independent of velocity. The same type of normalization can be used to determine the total and static pressures. This pressure coefficient normalization procedure is demonstrated below, and in the next section, it is used to form the basis of the seven-hole probe calibration technique.

As shown in reference 7, (the first description in the literature of the multihole probe pressure coefficient normalization technique), for a five-hole probe with the center hole pressure labeled as P_1 and the off-axis holes labeled as P_2, P_3, P_4, and P_5, the four pressure

coefficients are given by

$$C_{P_\alpha} = \frac{P_4 - P_5}{P_1 - \overline{P}} \qquad C_{P_\beta} = \frac{P_2 - P_3}{P_1 - \overline{P}} \qquad C_{P_{total}} = \frac{P_1 - P_{total}}{P_1 - \overline{P}} \qquad C_{P_{static}} = \frac{\overline{P} - P_{static}}{P_1 - \overline{P}} \quad (1)$$

where

$$\overline{P} = \frac{1}{4}(P_2 + P_3 + P_4 + P_5) \quad (2)$$

The advantage of this approach to calibration is that the determination of four quantities, based solely on pressures measured by the multihole probe, uniquely define the flow angle of the probe and total and static pressure, hence the velocity vector. Normalization by $P_1 - \overline{P}$ has been incorporated in the majority of the multihole probe calibration procedures developed in recent years (refs. 8, 9, 10).

The question arises as to why this type of normalization works and what are its limitations. The original description reference 7 shows that for three and five-hole probes, when the above normalization is used, the direction pressure coefficient C_{P_α} collapses on a straight line (within experimental uncertainty) for flow angles up to 30° as the Reynolds number is varied. No theoretical basis for the normalization procedure was given aside from the fact that $P_1 - \overline{P}$ is about one-half of the total pressure.

Additional insight into the velocity invariance of this type of normalization can be found by considering a model problem of flow past a two-dimensional (2-D) circular cylinder (yawmeter) with three pressure taps located as shown in figure 1. If the Reynolds number is much greater than 1, the flow on the windward side of the cylinder can be considered to be a potential flow with the pressure coefficient, at any point defined by θ, given by

$$C_P = \frac{P - P_\infty}{\frac{1}{2}\rho {U_\infty}^2} = 1 - 4sin^2(\theta - \beta) \quad (3)$$

A yaw angle calibration pressure coefficient can be defined as

$$C_{P_\beta} = \frac{P_3 - P_2}{P_1 - \overline{P}} \quad (4)$$

where

$$\overline{P} = \frac{1}{2}(P_2 + P_3) \quad (5)$$

After defining the angle η (pressure tap location) and substitution, the expression for C_{P_β} is

$$C_{P_\beta} = \frac{4cos\beta sin\beta}{tan\eta(cos^2\beta - sin^2\beta)} \quad (6)$$

The significance of this result is that C_{P_β} is dependent solely on the pressure hole location and the yaw angle. Additional dimensionless coefficient expressions can be formed, which are also explicitly velocity independent, but can be used to determine the vector magnitude of the velocity.

$$C_{P_{static}} = \frac{\overline{P} - P_{static}}{P_1 - \overline{P}} \qquad C_{P_{total}} = \frac{P_1 - P_{total}}{P_1 - \overline{P}} \tag{7}$$

The theoretical expressions for these coefficients as derived for the 2-D cylinder model problem are

$$C_{P_{static}} = \frac{1 - 4(sin^2\eta cos^2\beta + cos^2\eta sin^2\beta)}{4sin^2\eta(2cos^2\beta - 1)} \qquad C_{P_{total}} = \frac{-sin^2\beta}{sin^2\eta(2cos^2\beta - 1)} \tag{8}$$

The Bernoulli equation can be used with the static and total pressures to determine the vector magnitude of velocity ($n = 1$ for yaw meter).

$$| \vec{V} | = [(\frac{2}{\rho})(P_n - \overline{P})(1 + C_{P_{static}} - C_{P_{total}})]^{\frac{1}{2}} \tag{9}$$

If the flow angle β is small and the hole separation angle η is chosen to be 30^o then the calibration coefficient expressions can be simplified to

$$C_{P_\beta} = 4\sqrt{3}\beta \qquad C_{P_{static}} = -3\beta^2 \qquad C_{P_{total}} = -4\beta^2 \tag{10}$$

Shown in figure 2 is a comparison between the analytical expressions (eqs. 6 and 8), the small angle expressions (eq. 10), and experimentally measured coefficients (eqs. 4 and 7) for a 30^o yaw probe. The measured coefficients are based on surface pressure data taken by a single pressure tap on a cylinder which was rolled 360^o about its axis in 1^o increments (see fig. 3). This experimental data can be used to determine the equivalent response of a cylindrical (3-hole) yaw probe at any angle of yaw and hole configuration.

If the flow angle exceeds approximately 25^o for this probe, the calibration begins to fail. As can be seen in figure 4, the spread in the experimentally measured C_{P_β} becomes appreciable for large flow angles. This is not surprising considering that C_{P_β} at large angles is computed using pressure data which has a significant velocity dependence (see fig. 3) and deviates from a potential flow.

These results can be extended to configurations other than circular cylinders (e.g., spheres and cones). It appears that, in general, coefficients which are independent of velocity (to within experimental error), may be formulated based on the ratio of two pressure differences,

measured on an aerodynamic shape which obeys the equations of potential flow (or flows where the effects of viscosity are minimal). As will be shown, seven-hole probe calibration theory operates on the same basic principles as flow past a three-hole yaw meter and similarly, potential flow models can be used to predict the probe response.

There are some practical concerns such as measurement inaccuracies and the effects of probe flow separation (a viscous effect) which also must be considered when choosing probes and developing calibration schemes. Several of these difficulties will be addressed in the following sections for a seven-hole probe. One advantage to developing analytical and small angle models for probe response is that it becomes possible to determine the sensitivity of the probe and the accuracy of the measured data. The results of a simple error analysis for the three-hole yaw meter are presented in figure 5. This error estimate was derived using standard error estimation techniques (explained in greater detail in a later section of this paper), equations 4 and 7, and a pressure measurement resolution of 0.005 in. of H_2O. This result shows (see fig. 5) that the flow angle and the velocity magnitude measuring accuracy of the cylindrical yaw-meter vary parabolically with the flow angle.

3.2 Calibration Procedure For Seven-Hole Probes

The motivation for the development of the seven-hole probe techniques outlined in this report was the desire to investigate the flow field on the lee side of a body of revolution at angle of attack. In order to cover the complete anticipated flow angle range, it was necessary to use a probe which was raked ($\gamma = 30^\circ$) from the horizontal as shown in figure 6. The diameter of the probe was 0.125 in. and the half-angle of the conical tip was 45.0°. Also presented in figure 6 is the hole-numbering convention and definition of the relevant probe rotation angles.

The calibration was carried out in situ in a 15 by 15 in. low turbulence suction-type wind tunnel (see fig. 7). A microstepping motor-driven mechanism (25,000 microsteps per revolution) was used to accurately rotate the probe to known angles to the flow while maintaining the position of the probe tip as close to the wind tunnel centerline as possible. The rotation sequence used to position the probe involved pitching the probe through an angle θ in the wind tunnel x-z plane and then rotating the probe through an angle ψ about the probe stem (see fig. 6). This rotation sequence was chosen to minimize the mechanical complexity of the probe angular positioning mechanism. The angle of attack and sideslip angles of the probe (relative to the wind tunnel coordinate system) are given by

$$\alpha = sin^{-1}\left(\frac{cos\theta cos\psi sin\gamma + sin\theta cos\gamma}{cos\beta}\right) \tag{11}$$

$$\beta = sin^{-1}(-cos\theta sin\psi) \tag{12}$$

As can be seen from these expressions, for small θ and ψ angles (less than 15°) θ and -ψ are approximately equal to α and β for an unraked probe ($\gamma = 0$).

The approach to calibrating a seven-hole probe is similar in theory to the calibration procedure developed in reference 7 for five-hole probes. The difference between five- and seven-hole probe calibration is that only selected combinations of seven-hole probe holes are used to define the four unknown calibration coefficients whereas all the holes of a five-hole probe are used. The impact of using certain combinations of holes is that the useful flow angle range of the probe is greatly extended over that of a five-hole probe of similar geometry but the calibration complexity is increased.

At flow angles exceeding approximately 30°, the flow on the lee side of most probes will begin to separate. Calibration coefficients based on the pressure variations sensed by holes located beneath the separated region will no longer uniquely determine the flow angle of the probe (probe coefficients become multi-valued). To avoid this situation, a sectoring scheme such as that described in reference 2 may be devised which selects combinations of holes for which the flow is attached. The calibration coefficients are formed by using the hole that is sensing the maximum pressure and the holes adjacent to the maximum pressure hole. This process is referred to as choosing the probe sector.

The calibration procedure involves positioning the probe at known pitch and yaw angles to the flow and then measuring the seven pressures. Using the normalizing procedure based on principles developed in reference 7, and discussed in the previous section, pressure coefficients can be defined which are dependent on flow angle and insensitive to variations in the magnitude of the velocity (similar in form to eq. 4). For seven-hole probes, a total of 12 dimensionless pressure coefficients (2 for each sector) for the flow angularity are formed for use at high flow onset angles, (greater than approximately 20°) as described in reference 2.

$$C_{P_{r_1}} = \frac{P_1 - P_7}{P_1 - \frac{P_2+P_6}{2}} \qquad C_{P_{t_1}} = \frac{P_6 - P_2}{P_1 - \frac{P_2+P_6}{2}} \tag{13}$$

$$C_{P_{r_2}} = \frac{P_2 - P_7}{P_2 - \frac{P_1+P_3}{2}} \qquad C_{P_{t_2}} = \frac{P_1 - P_3}{P_2 - \frac{P_1+P_3}{2}} \tag{14}$$

$$C_{P_{r_3}} = \frac{P_3 - P_7}{P_3 - \frac{P_2+P_4}{2}} \qquad C_{P_{t_3}} = \frac{P_2 - P_4}{P_3 - \frac{P_2+P_4}{2}} \tag{15}$$

$$C_{P_{r_4}} = \frac{P_4 - P_7}{P_4 - \frac{P_3+P_5}{2}} \qquad C_{P_{t_4}} = \frac{P_3 - P_5}{P_4 - \frac{P_3+P_5}{2}} \tag{16}$$

$$C_{P_{r_5}} = \frac{P_5 - P_7}{P_5 - \frac{P_4+P_6}{2}} \qquad C_{P_{t_5}} = \frac{P_4 - P_6}{P_5 - \frac{P_4+P_6}{2}} \tag{17}$$

$$C_{P_{r_6}} = \frac{P_6 - P_7}{P_6 - \frac{P_5+P_1}{2}} \qquad C_{P_{t_6}} = \frac{P_5 - P_1}{P_6 - \frac{P_5+P_1}{2}} \tag{18}$$

In reference 2, the direction-sensitive coefficient nomenclature contains a reference to the flow direction θ and ψ ($C_{P_{\theta_1}}$, for example). This convention is inappropriate in the present

context because of the strong coupling between the direction coefficients. As a result, the subscripts r (for radial pressure difference) and t (for tangential pressure difference) have been used to distinguish between the two direction-sensitive coefficients.

The total and static pressure coefficients are also dependent on the sector and are defined as follows.

$$C_{P_{total_1}} = \frac{P_1 - P_{total}}{P_1 - \frac{P_2+P_6}{2}} \qquad C_{P_{static_1}} = \frac{\frac{P_2+P_6}{2} - P_{static}}{P_1 - \frac{P_2+P_6}{2}} \tag{19}$$

$$C_{P_{total_2}} = \frac{P_2 - P_{total}}{P_2 - \frac{P_1+P_3}{2}} \qquad C_{P_{static_2}} = \frac{\frac{P_1+P_3}{2} - P_{static}}{P_2 - \frac{P_1+P_3}{2}} \tag{20}$$

$$C_{P_{total_3}} = \frac{P_3 - P_{total}}{P_3 - \frac{P_2+P_4}{2}} \qquad C_{P_{static_3}} = \frac{\frac{P_2+P_4}{2} - P_{static}}{P_3 - \frac{P_2+P_4}{2}} \tag{21}$$

$$C_{P_{total_4}} = \frac{P_4 - P_{total}}{P_4 - \frac{P_3+P_5}{2}} \qquad C_{P_{static_4}} = \frac{\frac{P_3+P_5}{2} - P_{static}}{P_4 - \frac{P_3+P_5}{2}} \tag{22}$$

$$C_{P_{total_5}} = \frac{P_5 - P_{total}}{P_5 - \frac{P_4+P_6}{2}} \qquad C_{P_{static_5}} = \frac{\frac{P_4+P_6}{2} - P_{static}}{P_5 - \frac{P_4+P_6}{2}} \tag{23}$$

$$C_{P_{total_6}} = \frac{P_6 - P_{total}}{P_6 - \frac{P_5+P_1}{2}} \qquad C_{P_{static_6}} = \frac{\frac{P_5+P_1}{2} - P_{static}}{P_6 - \frac{P_5+P_1}{2}} \tag{24}$$

At low angles, (less than approximately 30°) the flow is fully attached on the tip of the probe. Under these conditions, greater probe sensitivity may be obtained by using pressures measured by all seven holes. Two coefficients may be defined, based on a linear combination (see ref. 2 for further details) of the following three velocity-invariant coefficients.

$$C_{P_{t_a}} = \frac{P_4 - P_1}{P_7 - \overline{P}} \qquad C_{P_{t_b}} = \frac{P_3 - P_6}{P_7 - \overline{P}} \qquad C_{P_{t_c}} = \frac{P_2 - P_5}{P_7 - \overline{P}} \tag{25}$$

where

$$\overline{P} = \frac{1}{6}(P_1 + P_2 + P_3 + P_4 + P_5 + P_6) \tag{26}$$

At low angles, the following expressions are used (as derived in ref. 2)

$$C_{P_{\alpha_7}} = C_{P_{t_a}} + \frac{C_{P_{t_b}} - C_{P_{t_c}}}{2} \qquad C_{P_{\beta_7}} = \frac{1}{\sqrt{3}}(C_{P_{t_b}} + C_{P_{t_c}}) \tag{27}$$

The static and total pressure coefficients at low angles are given by

$$C_{P_{total_7}} = \frac{P_7 - P_{total}}{P_7 - \overline{P}} \qquad C_{P_{static_7}} = \frac{\overline{P} - P_{static}}{P_7 - \overline{P}} \tag{28}$$

The expressions for the sector 7 flow-direction calibration coefficients listed above have been expressed in terms of α and β (not r and t as before). The reason for this is that the linear combination of the three $C_{P_{...}}$ coefficients shown above is formed in such a way as to maximize the calibration coefficient sensitivity to changes in α and β.

In order to determine which sector to use when measuring in an unknown flow field, the seven measured pressures are compared to each other. The sector (set of four holes) is chosen based on which hole has the highest pressure. The presence of any flow separation at the tip hole is then checked for by comparing P_7 with the remaining three holes on the lee side of the probe. When the flow is attached, the lee side holes register pressures that are less then P_7. If the difference between P_7 and the three leeward pressures is less than the chosen tolerance, then the flow at the tip hole number 7 is separated and the probe is out of the flow angle range. In addition to the tip-hole separation test, a second separation test is necessary. At high angles, the vortical flow on the lee side of the probe tip can induce a higher pressure than that of the center hole P_7, hence, causing the previously mentioned test to fail. If at least three of the off-center pressures (P_1 through P_6) are less than P_7 then the tip-hole separation check is valid. These tests may seem to be a bit awkward, nevertheless they are necessary in order to prevent double-valued calibration coefficients and hence erroneous flow-angle determination during data acquisition.

The calibration procedure follows.

1. The probe is rotated to a known angle and the seven pressures (referenced to the tunnel wall static) and a tunnel reference condition (the total pressure) are recorded.

2. At each probe position, the 28 calibration coefficients (4 for each sector) are computed and stored along with the θ and ψ angular probe position.

The probe should be calibrated over the entire anticipated range of probe flow angles. Typically, an angular increment of 5^o is satisfactory. In the present study, the incremental change in angle was 5^o covering a range of θ angles from -30^o to 80^o and ψ angles of -80^o to 80^o.

The procedure for using a calibrated probe to obtain the three components of velocity is as follows.

1. The seven pressures and tunnel reference pressure are measured.

2. The probe sector is chosen based of the relative magnitudes of the recorded pressures.

3. The four pressure coefficients of the chosen sector are computed.

4. The probe flow-separation criteria are applied.

5. The unknown probe flow angles θ and ψ are determined by using the Akima interpolation method (an IMSL subroutine; based on the method of ref. 11) to interpolate the C_{P_r},

C_{P_t} calibration data, at the measured values of C_{P_r}, C_{P_t}, for the flow angle θ, ψ. The Akima method uses fifth-degree interpolating polynomials and has continuous first derivatives.

6. The magnitude of the velocity is determined by interpolation of $C_{P_{total}}$, and $C_{P_{static}}$, at the θ, ψ flow angles found in step 5 and then solving for P_{total} and P_{static}. Equation 9 is then used with P_n (the pressure of the selected hole), and $\overline{P}$. ($\overline{P} = \frac{P_2+P_4}{2}$, for sector 3, for example).

7. The final step is to use θ, ψ and $\mid \vec{V} \mid$ to determine the velocity components in the wind tunnel coordinate system. The velocity components in the wind-tunnel reference system are

$$u = \mid \vec{V} \mid cos(\theta - \gamma) cos(\psi) \tag{29}$$

$$v = \mid \vec{V} \mid sin(\theta - \gamma) \tag{30}$$

$$w = - \mid \vec{V} \mid cos(\theta - \gamma) sin(\psi) \tag{31}$$

As mentioned previously, the advantage of the sector approach is that it extends the angular range of the probe by using pressures sensed by holes where the flow is Reynolds number invariant. An illustration of this principle is shown in figure 8. In this figure, the effect of velocity on C_{P_r} is presented as ψ is varied for a seven hole probe at constant θ, where $\Delta C_{P_r} = C_{P_r} - \overline{C_{P_r}}$ and $\overline{C_{P_r}}$ is the average of C_{P_r} for the six velocities tested at each position. At low angles, the sectoring scheme chooses sector 7 (the low angle sector) and as can be seen, the spread in the data is minimal for ψ less than 30°. At high angles, sector 5 is chosen for angles greater than 30°, and the data collapses onto one line. The reason the velocity invariance fails for sector 7 at large ψ is the flow separation over a portion of the probe tip. The failure of the sector 5 data at low angles can be attributed to measurement inaccuracies. As can be seen in figure 4, for the yaw meter, the quantity equivalent to $P_5 - (P_4 + P_6)/2$ becomes small; hence minor inaccuracies can have a significant impact on C_{P_r}.

Shown in figure 9 is a $\theta - \psi$ map of the sectors chosen by the calibration scheme. The symbols indicate the hole registering the greatest pressure. The boundaries on the right-hand-side of this figure are the flow angle limitations as enforced by the two-probe flow separation tests applied to the calibration data. A ballpark figure for the maximum allowable ς resultant flow angle is approximately 70° to 80° for the 45.0° conical-tip seven-hole probe.

Presented in figure 10 are the four calibration coefficients for each sector. These data give a visual indication of the probe sensitivity to flow angle. Regions of high probe flow-angle sensitivity have greater spacing of the C_{P_t}, C_{P_r} data points in figures 10a and 10b. As the flow angle increases, the probe sensitivity to the flow angle decreases. At low flow-onset angles, the pitch and yaw direction are only weakly coupled as shown by the relatively straight intersecting lines in figure 10a. At high flow-onset angles, the C_{P_t}, C_{P_r} variations are nonlinear and strongly coupled.

Once the flow angle has been determined by interpolation of the data in figure 10 (a,b) the static and total pressure coefficients are found by interpolation of the data shown in figure 10 (c-f).

This approach to seven-hole probe calibration has been used in a study of the lee side flow field on an ogive-cylinder at high angle of attack. Presented in figure 11 are the crossflow plane velocity vectors at $x/L = 0.95$ on a $L/D = 3.5$ ogive with a $L/D = 1.0$ cylindrical afterbody at $\alpha = 30^o$ and $Rn_L = 820{,}000$. This data were measured in the 15-in.-by-15-in. wind tunnel (fig. 7) and is discussed in greater detail in reference 12.

3.3 Pressure Probe Analytical Model

Typically, as shown in the previous section, seven-hole pressure probe calibration curves are nonlinear at large probe incidence angles. This nonlinearity may lead to low probe sensitivity for certain flow-onset angles. This situation may be avoided by using an analytical model to predict probe characteristics and tailor the probe geometry for specific applications.

As shown in a previous section of this paper and also in reference 13, the flow around a pressure probe can be modeled using potential flow theory. In reference 13, a 3-D analysis of the behavior of static-pressure probes was studied by using a panel method. The objective of this study was to find a static pressure probe geometry which is made insensitive to yaw and angle of attack by contouring of the probe cross-section. Wind tunnel tests of four computer-aided probe designs showed that this objective was accomplished, but no direct comparisons of the predicted and measured probe response were presented.

In reference 14, the flow around a conical probe was modeled using slender body theory. The effect of pitch and yaw angle variation was included through superimposing the flow at $\alpha = 0.0^o$ and $\alpha = 90.0^o$ and a general expression for the pressure at any point on the probe surface was derived from theory. The slender-body results produced the expected trends in differential pressure with variation in flow onset angle, but again, no direct comparison with experiment was presented.

In the present study, the approach to modeling pressure probe behavior was to combine the approaches used in the two aforementioned references. The panel method approach is preferred over the slender body approach due to the severe limitations imposed by slender-body theory near the probe tip (dR/dz must be much less than 1); on the other hand, the simplicity of slender body theory makes it desirable from a probe optimization point of view.

Before the final modelling approach was decided upon several slender body methods were tried including the methods presented in references 14 and 15. There were slight differences in the pressure distribution results of the various methods with the method of reference 15 giving the best results (results described below are based on the method of reference 15).

An example of the inability of slender-body theory to predict the pressure distribution near the tip of a shape which is similar to a typical pressure probe geometry is shown in figure 12a. This figure presents a comparison of the tip pressure variation with the x-position for a cone with a cylindrical afterbody at $\alpha = 0^o$ as predicted by a panel method, slender-body theory, and as measured in an experiment (experimental data from ref. 16). As can be seen, the slender-body theory result is in error by a significant amount in the region where the greatest accuracy is required for probe modeling. The pressure peak at $x/D = 2.8$ is captured well by Panair while there is virtually no indication of this pressure peak in the slender body results. Shown in figure 12b is a comparison of the tip pressure variation with x-position for a L/D = 10 prolate spheroid at $\alpha = 0^o$. For this case, the data compare favorably aside from what appears to be a small static-pressure offset error in the experimental data of reference 17. These figures demonstrate that slender body theory is sufficient for bodies with continuous, slowly varying shapes but is highly inaccurate for the types of geometries which are common to multihole pressure probes. On pointed bodies, singular behavior of the slender body equations at the tip causes substantial deviations from the actual tip pressure.

In order to avoid computing a panel method solution for every onset flow angle, a modified form of the superposition of the two-potential-flow solutions approach used in reference 14 has been applied. The model is quite general and can be applied to most probes which are bodies of revolution.

The analytical model is based on the assumption that the flow around the probe is a potential flow. At first glance, this may not seem to be a good approximation considering that the flow separates from most probe tips at flow angles greater than 30°. As has been shown, multihole probe calibration techniques fail when a pressure is used that is measured in regions where the flow is separated. In regions where the flow is attached, the potential flow is a good approximation of the real flow.

The computer program PANAIR (see ref. 18) has been used to find the potential flow solutions required by the probe model. This panel method solves Laplace's equation for the total velocity potential Φ by superimposing quadratically varying doublet and linearly varying source singularities on paneled portions of the boundary surface. The governing equations and boundary conditions are

$$\vec{\nabla}^2\Phi = 0 \tag{32}$$

$$\vec{\nabla}\Phi = \vec{V}_\infty \quad at \ \infty \tag{33}$$

$$\vec{\nabla}\Phi \cdot \vec{\nabla}F = 0 \quad on \ F(r,\theta,z) = 0 \tag{34}$$

where

$$\vec{V} = \vec{\nabla}\Phi \tag{35}$$

The solution for a body at an arbitrary angle of attack and sideslip can be found by forming a linear combination of the solution at $\alpha = 0^o$ and $\alpha = 90^o$. If Φ^1 is the solution at $\alpha = 0^o$ and Φ^2 is the solution at $\alpha = 90$, then the solution at any α is given by

$$\Phi = \Phi^1 cos(\alpha) + \Phi^2 sin(\alpha) \tag{36}$$

It can be seen, by substitution, that this expression satisfies the governing equations and boundary conditions for a body of revolution at angle of attack. To find Φ at a given α and β for a body of revolution, a coordinate transformation may be used. This transformation is equivalent to a rotation of the freestream velocity vector through an angle χ to the $x - z$ plane as shown in figure 13. The transformation from the r, θ, z coordinate system to the r, ξ, z system is defined by

$$\xi = \theta + \chi \tag{37}$$

where

$$\chi = tan^{-1}[\frac{sin(\beta)}{cos(\beta)sin(\alpha)}] \tag{38}$$

Correspondingly, the angle of attack is redefined and a new angle of attack ς is used in conjunction with the expression for Φ to determine the velocity potential for a pitched and yawed body of revolution.

$$\varsigma = cos^{-1}[cos(\alpha)cos(\beta)] \tag{39}$$

The pressure coefficient is given by

$$C_P = \frac{P - P_\infty}{\frac{1}{2}\rho {U_\infty}^2} = 1 - \frac{|\vec{V}|^2}{V_\infty^2} = 1 - \frac{|\vec{\nabla}\Phi|^2}{V_\infty^2} \tag{40}$$

No additional approximation is involved in this superposition and transformation of the potential flow solution. This technique should be generally applicable to any body of revolution where the potential flow solution is desired at an arbitrarily chosen flow onset angle.

A comparison of the computed and measured pressure variation with yaw angle at $\theta = 0$, for the seven-hole probe is shown in figure 14. The trends and magnitudes of the computed pressure coefficients agree fairly well with the experimental values. The main differences are as follows.

1. The experimental pressure distribution drop-off with β of the tip hole (hole 7) is not as dramatic as the computational drop-off. Possibly, this may be caused by small differences in the actual and modeled tip geometries.

2. The peak pressure computed by hole 5 near $\beta = -40^o$ and hole 3 near $\beta = 40^o$ slightly less than the measured value. Considering that the half-angle of the conical probe is 45.0^o,

it is expected that these peaks should be close to stagnation pressure. as is the case with the experimental data.

3. At large negative yaw angles, the computed pressure of hole 2 is substantially higher than the experimental results. This discrepancy is evidence of flow separation on the lee side of the probe. Typically, when the flow separates on a body of revolution, the suction developed on the lee side of the body is greater than that predicted by the potential flow, owing to the presence of lee-side vortices. Similar pressure trends are shown for hole 6 at large yaw angles and also for the other holes at different pitch angles.

Shown in figure 15 are the analytically determined calibration coefficients for the seven-hole probe. These curves can be compared with the experimental calibration data presented in figure 10. There are differences, but the general trends and magnitudes of the two results are close enough to be of value to probe designers.

3.4 Error Analysis

An analysis was performed to determine the uncertainty of the present seven-hole probe velocity component determination. The analysis included uncertainty of the pressure transducer calibration, uncertainty of the seven-hole probe calibration, uncertainty in the measurement of flow angle, and velocity magnitude using the calibrated seven-hole probe.

Following fairly standard error analysis procedures (see ref. 19), an estimate of the total precision (zero-centered) error in a measurement may be made by using the constant odds combination given by

$$\delta R = \sqrt{\sum_{i=1}^{n} \left(\frac{\partial R}{\partial e_i} \delta e_i\right)^2} \tag{41}$$

All bias errors such as pressure transducer temperature drift and probe stem deflection have been corrected for or neglected, hence they are not included in the analysis. In an actual measurement situation, bias errors can be the dominant error source and care must be taken to reduce the influence of these errors to a minimum.

The pressure transducer is calibrated by first reading the analog-to-digital (A/D) counts with zero pressure applied (c_z) followed by applying a known pressure difference (as measured by a manometer (h)), and reading the corresponding A/D counts (c_{ref}). An unknown pressure can then be determined from

$$P = \frac{h}{(c_{ref} - c_z)}(c - c_z) \tag{42}$$

An estimate of the pressure transducer calibration error may be made using equations 41 and 42 and the identified sources of error and their estimated magnitude.

Inaccuracies in the reference pressure due to manometer reading uncertainties (0.001 in. H_2O) and a one-count A/D conversion uncertainty are the main factors which have been included in the pressure transducer analysis. The combined effect of these errors leads to a 0.046-in. H_2O pressure measurement uncertainty.

Owing to the complexity of the seven-hole probe calibration process (see equations given in the Calibration Procedure) and the fact that the pressure measurement error propagates through the measurement-chain, uncertainty analysis of the seven-hole probe calibration is considerably more complicated than the pressure transducer analysis. To grapple with these difficulties, the "jitter"approach, as discussed by Moffat (ref. 19), was used. The eight measured pressures at each calibration angle were numerically varied by small known amounts. The resulting variations of the calibration coefficients from their original values are used to determine the $\partial C_{P...}/\partial e_i$ terms of equation 41. With use of the appropriate δe_i values, the total uncertainty of the calibration coefficients can be determined. The factors included were uncertainty in pressure measurement and a one-count A/D error (a 12-bit resolution A/D was used). Angular positioning errors were assumed to be negligible due to the high accuracy of the 25,000 microstep per revolution positioning mechanism. The result of this part of the analysis is $\delta C_{p...}$ which is the error in the calibration coefficients due to the combined effects of the pressure measurement error and errors associated with the probe calibration.

The uncertainty in the seven-hole probe measurement of velocity in an unknown flow field (the end goal of this analysis) is dependent on the errors accumulated during the probe calibration process and also the errors associated with the actual measurement using the calibrated probe. The jitter approach has also been used to estimate these errors in a manner similar to the calibration coefficient error analysis.

The uncertainty in the velocity magnitude determination is directly impacted by the accuracy of the flow angle determination. As discussed in the calibration procedure section, the velocity magnitude is determined by interpolating for $C_{P_{total}}$ and $C_{P_{static}}$ at the measured flow angle and then using these values to compute the velocity magnitude.

The error associated with interpolation of the calibration data is dependent on the degree of nonlinearity of the calibration data and the truncation error of the interpolation scheme. The magnitude of these errors can be estimated by applying the interpolation process to a model equation which is based on the calibration data. The procedure for estimating the error involved fitting a polynomial to the calibration data (the model equation), evaluating the polynomial at the flow angle base points of a typical probe calibration, and then computing the rms error which arises when the interpolation approach is applied to the modelled calibration data. Several interpolation schemes were tried and it was decided that the Akima method, which can handle irregularly spaced data points, and is accurate, was a good choice.

One of the major differences between the calibration method presented in reference 3 and the present approach is the use of polynomial calibration coefficient expressions (in ref.

3), as opposed to the interpolation approach used herein. The Akima interpolation scheme was chosen because it was felt that the deviations (in some cases as high as a 1.3° flow angle discrepancy) could not be attributed to physical causes in the least-squares curve-fit calibration data shown in reference 3. The Akima interpolation method is a weighted-nearest-neighbors method which should be more accurate than curve-fit methods based on equal weighting of all of the calibration data across the complete flow angle range.

In general, experimental data should be assumed to be correct unless the deviations in the expected trends of data can be justified on theoretical grounds or be attributed to experimental error. The error analysis of the present calibration procedure did not turn up errors of this magnitude; hence the least-squares polynomial approach (used in ref. 3) was probably the greatest source of error which could be significantly reduced.

Shown in figure 16 are the flow angle and velocity magnitude error predicted by the foregoing analysis. As can be seen, the angle error varies parabolically (θ is constant for each symbol type) with the flow angle ψ, which is similar to the three-hole yaw meter results. The trend of the velocity magnitude error is not similar to the three-hole yaw meter result owing to the different shapes of the $C_{P_{total}}$ and $C_{P_{static}}$ curves of the yaw meter and seven-hole probe.

The validity of the above analyses can be tested by positioning the calibrated probe at known angles to the flow and then measuring the velocity (or flow angles) repeatedly using the data system. If the uncertainty prediction is accurate, deviation of the velocity measurement should agree with the predicted precision errors. A probability density function of many samples should form a normal distribution about the known angle that the probe was positioned to. The importance of this validation is that once agreement is achieved, measurement system changes may be made in a systematic way to reduce the error.

The predicted values of the seven-hole probe velocity measurement are summarized in table 1. Since the sensitivity of the probe varies greatly over the onset flow angles studied, two error totals are given, one representative of low flow angles and a second for onset angles greater than 30°. These error values were determined by averaging over 700 error predictions covering the entire flow onset angle range.

TABLE 1.- UNCERTAINTY PREDICTION.

	Component	Predicted	Predicted	Units
		Low angles	High angles	
1	Pressure	0.046	0.046	in. H_2O
2	Angle	0.2	0.5	deg
3	Velocity	1	1	% U_∞

Wind tunnel mean speed drift or very-low-frequency speed variation can pose a problem during the seven-hole probe calibration. Typically, the seven pressures are not measured

simultaneously. During the scanning time between ports, the flow at the probe tip may change, causing an apparent change in measured flow angle. This error could be minimized through the use of multiple pressure transducers and simultaneous sampling of the seven pressures, although other errors associated with the calibration of multiple pressure transducers may be introduced. Wind tunnel flow angularity (typically, a 0.5° variation across the test section) can also affect the accuracy of probe calibration through changes in the freestream direction relative to the probe. This difficulty can be minimized by keeping the probe near the tunnel centerline during the calibration process. Ambient condition changes do not affect the flow angle measurements directly since the flow angle is determined from pressure coefficients which are ratios of pressure differences.

Certain steps can be taken to reduce the measurement error to levels lower than shown in table 1. The greatest gain in accuracy can be achieved by calibrating the pressure transducer using a manometer which can resolve down to at least a thousandth of an inch H_2O. Use of a 16-bit A/D converter (as opposed to a 12-bit A/D converter) will reduce the A/D errors to the point where they become insignificant in most cases.

As shown in figure 8, the spread in ΔC_p indicates that probe Reynolds number effects may be present but are small (within the flow angle limitations of the probe). Isolation of Reynolds number effects from other sources of error is difficult to accomplish and since these errors do not seem to contribute significantly to the total error, they have been neglected.

4. CONCLUSIONS

The seven-hole probe is a versatile and accurate instrument for measuring the three components of velocity in a flow field where the onset flow angle is high.

1. It has been demonstrated that the key to the success of many probe calibration techniques is the ability to define velocity invariant pressure coefficients which are the ratio of two pressure differences. This type of normalization is successful only when the flow over the probe is essentially a potential flow.

2. The seven-hole probe calibration is conceptually simple and is essentially a variation of a time-tested multihole probe technique.

3. The maximum probe onset-flow angle is approximately 70° for the present probe geometry. For flow angles greater than 70°, extensive flow separation occurs on the probe tip, causing the calibration coefficients to become double-valued and velocity dependent in violation of the assumptions of the calibration technique. As part of the data acquisition procedure, a simple probe-flow separation test, based on the relative magnitudes of the seven measured pressures, can be performed to insure the validity of the measurement.

4. Results of an error analysis show that the seven-hole probe of the present study can

measure angular variations to within approximately 0.5° and velocity magnitude to within 1.0 percent of the free stream. These error figures could be reduced significantly by reducing the 0.046-in.H_2O pressure measurement uncertainity of the present study.

5. A relatively accurate analytical model of the probe response, based on a unique application of a panel method, has been developed and should be useful to multihole probe designers.

REFERENCES

1. Bryer, D. W.; and Pankhurst, R. C.: *Pressure-Probe Methods for Determining Wind Speed and Flow Direction.* Her Majesty's Stationary Office, London, 1971.

2. Gallington, R. W.: *Measurement of Very Large Flow Angles with Non-Nulling Seven-Hole Probes.* USAFA-TR-80-17, 1980.

3. Everett, K. N.; Gerner, A. A.; and Durston, D. A.: Theory and Calibration of Non-Nulling Seven-Hole Cone Probes for Use in Complex Flow Measurement. AIAA Paper 82-0232, Jan. 1982.

4. Gerner, A. A.; and Maurer, C. L.: Calibration of Seven-Hole Probes Suitable for High Angles in Subsonic Compressible Flows. AIAA Paper 82-0410, Jan. 1982.

5. Everett, K. N.; Gerner, A. A.; and Durston, D. A.: Seven-Hole Cone Probes for High Angle Flow Measurement: Theory and Calibration. *AIAA J.*, vol. 21, no. 7, July 1983, p. 992.

6. Huffman, D.G.: Theory, Performance and Design of Flow Direction and Mach Number Probes. AFATL-TR-81-44, April 1981.

7. Krause, L. N.; and Dudzindki, T. J.: Flow-Direction Measurement with Fixed Position Probes in Subsonic Flows over a Range of Reynolds Number. NASA TMX-52576, May 1969.

8. Treaster, A. L.; and Yocum, A. M.: The Calibration and Application of Five-Hole Probes. *ISA Trans.*, vol. 18, no. 3, Mar. 1979, p. 23.

9. Westphal, R. V.; Pauley, W. R.; and Eaton, J. K.: Interaction Between a Vortex and a Turbulent Boundary Layer Part 1: Mean Flow Evolution and Turbulence Properties. NASA TM-88361, Jan. 1987.

10. Sitaram, N.; and Treaster, A. L.: A Simplified Method of Using Four-Hole Probes to Measure Three-Dimensional Flow Fields *J. Fluids Engineering* , vol. 107, Mar. 1985, p. 31.

11. Akima, H.: A Method of Bivariate Interpolation and Smooth Surface Fitting for Irregularly Distributed Data Points, *ACM Trans. Math Software 4*, vol. 2, June 1978, p. 148.

12. Zilliac, G. G.: A Computational/Experimental Study of the Vortical Flow Field on a Body of Revolution at Angle of Attack. AIAA Paper 87-2277-CP, Aug. 1987.

13. Smith, A. M. O.; and Bauer, A.,B.: Static-Pressure Probes That are Theoretically Insensitive to Pitch, Yaw and Mach Number. *J. Fluid Mech.*, vol. 44, part 3, 1970, p. 513.

14. Huffman, D.G.; Rabe, D.C.; and Poti, N.D.: Flow Direction Probes From a Theoretical and Experimental Point of View *J. Phys E: Sci. Instrum.*, vol. 13, 1980, p. 751.

15. Karamcheti, K.: *Principles of Ideal-Fluid Aerodynamics.* John Wiley and Sons, Inc., New York, 1966.

16. Hess, J. L.; and Smith A. M. O.: Calculation of the Potential Flow About Arbitrary Bodies *Progress in Aeronautical Sciences,* 8. Pergamon, 1966, p. 1.

17. Matthews, C.W.: A Comparison of the Experimental Subsonic Pressure Distributions About Several Bodies of Revolution With Pressure Distributions Computed By Means of the Linearized Theory. NACA TN 2519, Feb. 1952.

18. Johnson, F.T.; and Erickson, L.L.: A General Panel Method for the Analysis and Design of Arbitrary Configurations in Incompressible Flows. NASA CR-3079, June 1979.

19. Moffat, R. J.: Contributions to the Theory of Single-Sample Uncertainty Analysis *Trans. ASME*, vol. 104, June 1982, p. 250.

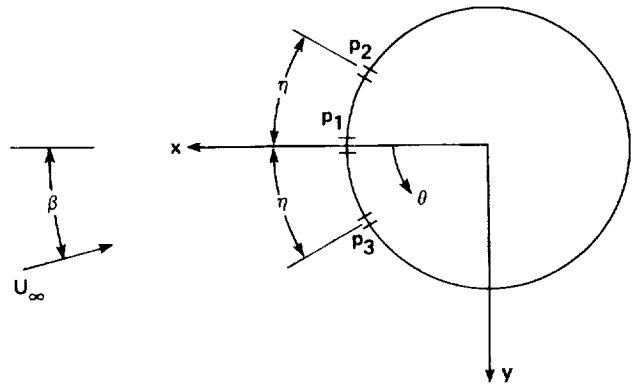

Figure 1.– Three-hole yaw meter.

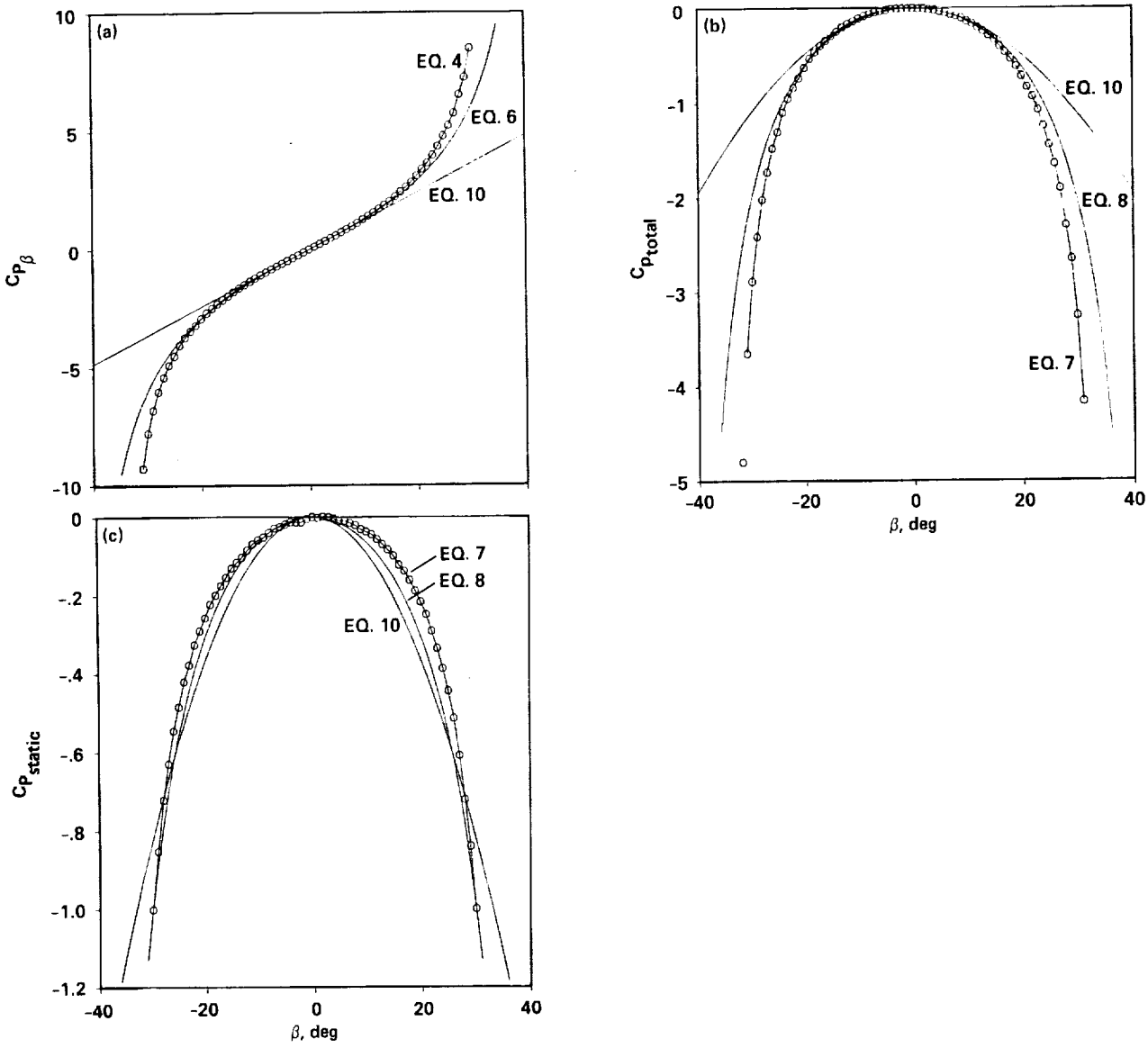

Figure 2.– Three-hole yaw meter. (a) Flow direction coefficient; (b) total pressure coefficient; (c) static pressure coefficient.

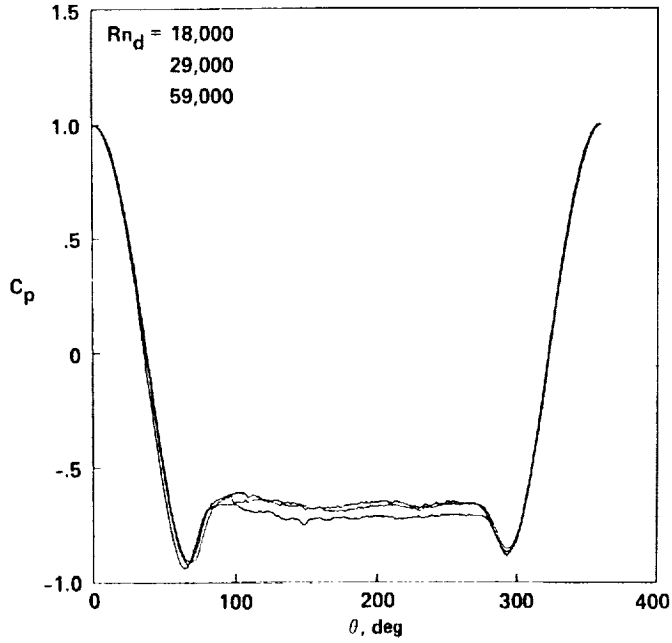

Figure 3.– Two dimensional circular cylinder pressure coefficient.

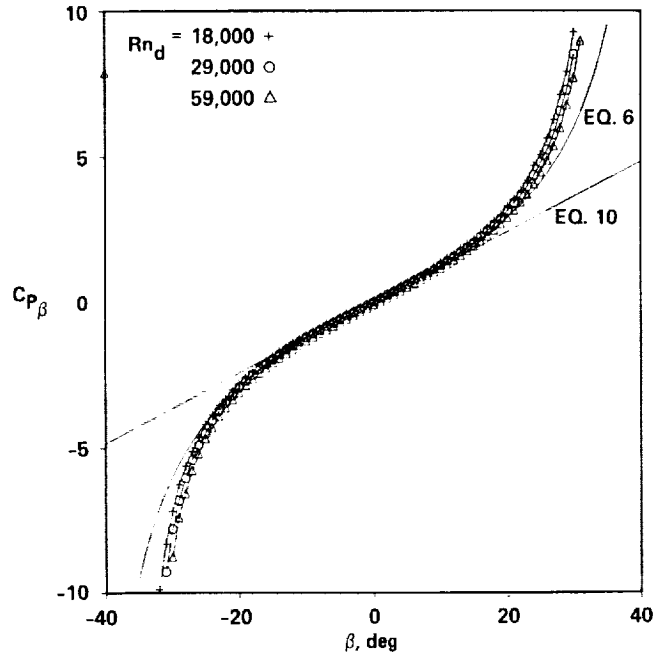

Figure 4.– Effect of velocity on the yaw meter direction coefficient.

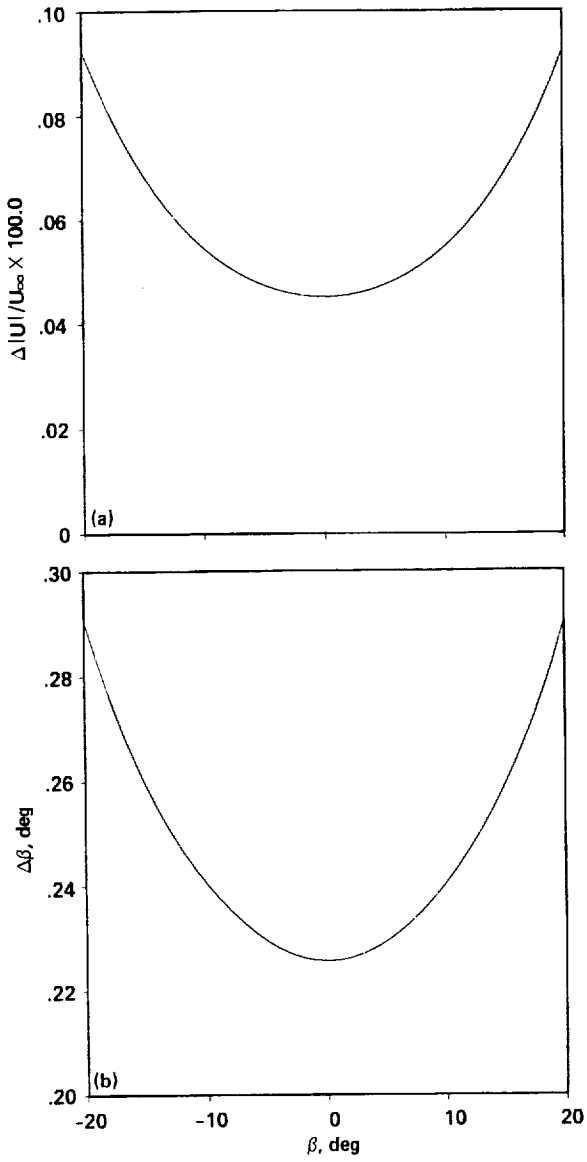

Figure 5.– Yaw meter error. (a) Flow angle error; (b) velocity magnitude error.

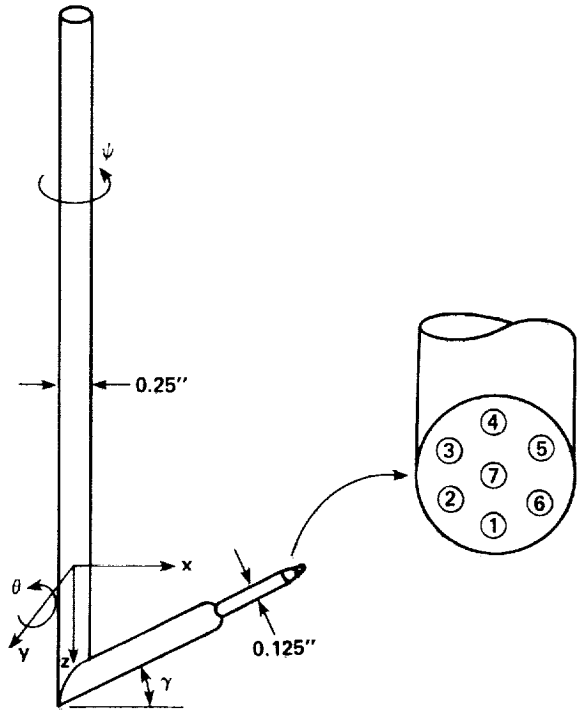

Figure 6.– Seven hole probe and hole numbering convention.

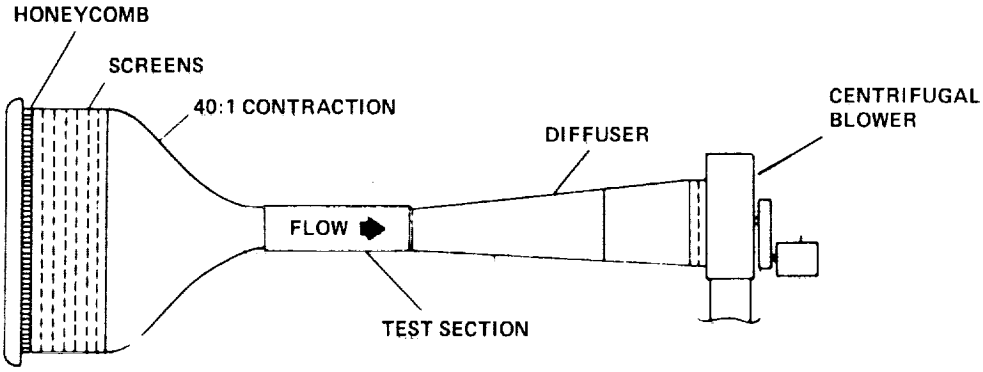

Figure 7.– The 15 × 15 inch low turbulence wind tunnel.

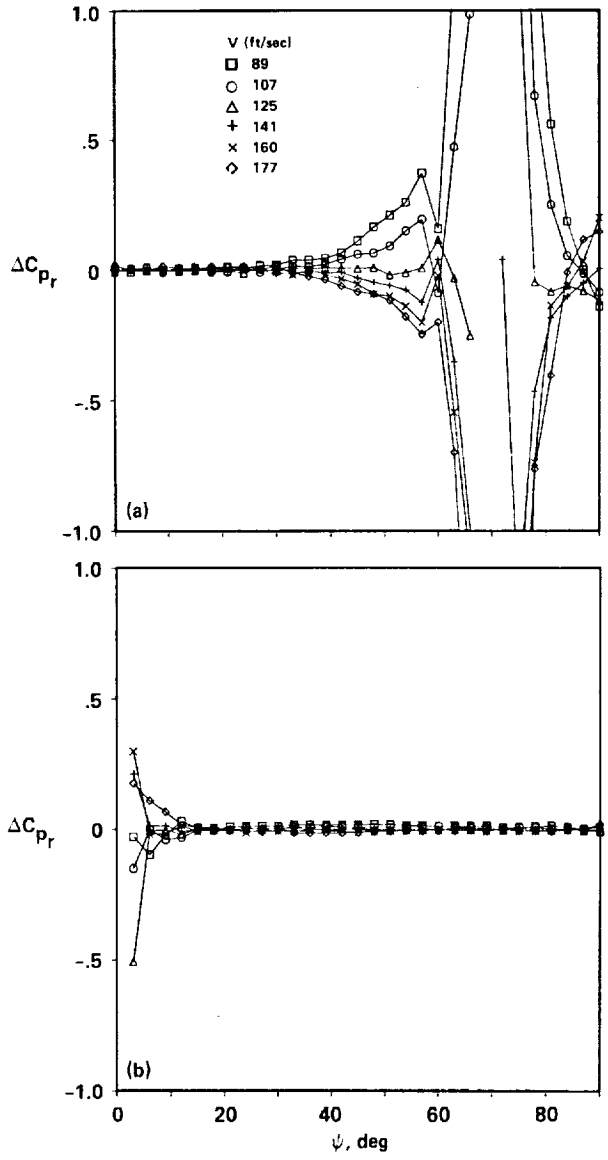

Figure 8.– Effect of velocity on seven-hole probe direction coefficient. (a) Sector 7; (b) sector 5.

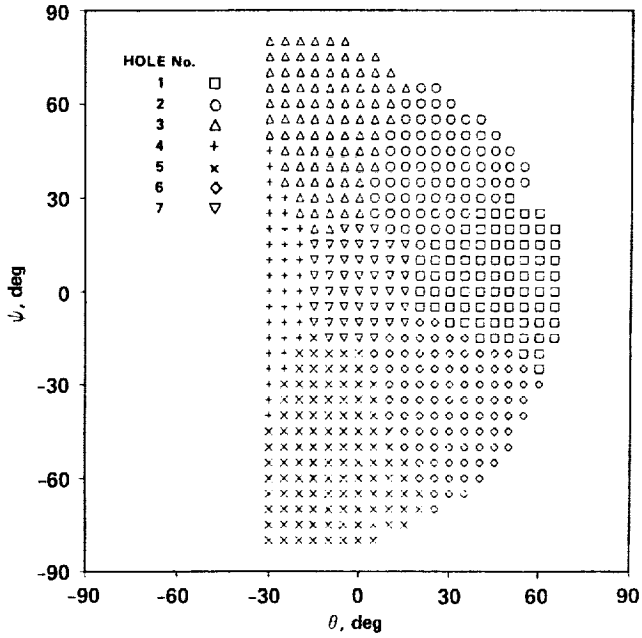

Figure 9.– Seven-hole probe sectors.

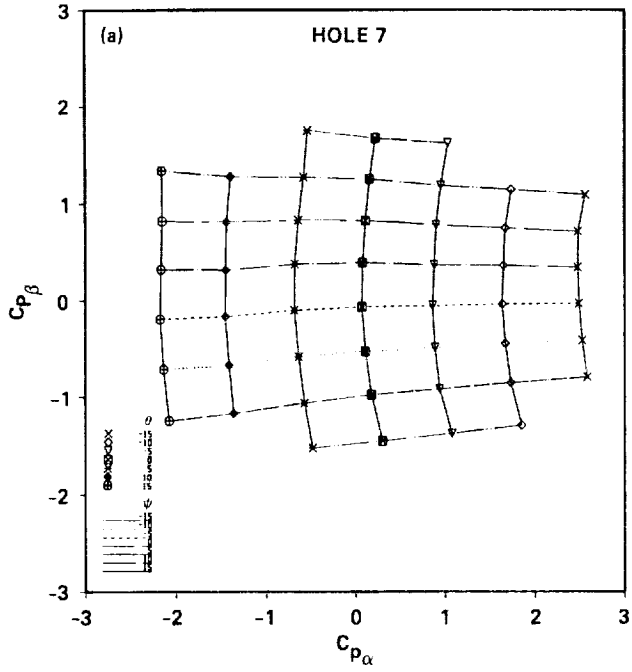

(a) Direction coefficients for hole 7 (low flow angle).

Figure 10.– Measured flow direction coefficients for a seven-hole probe (low flow angle).

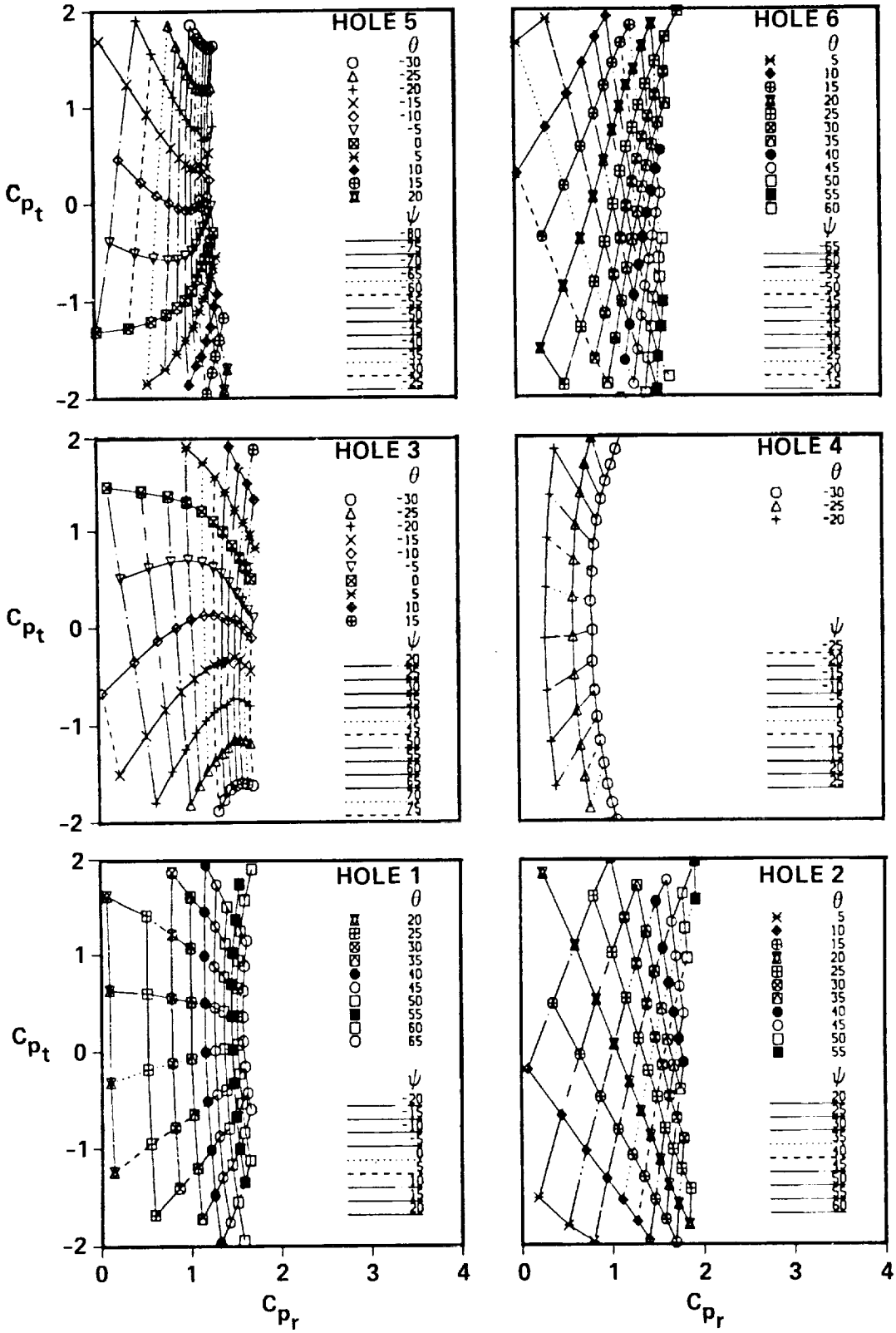

(b) Direction coefficients for holes 1 to 6 (high flow angle).

Figure 10.– Continued.

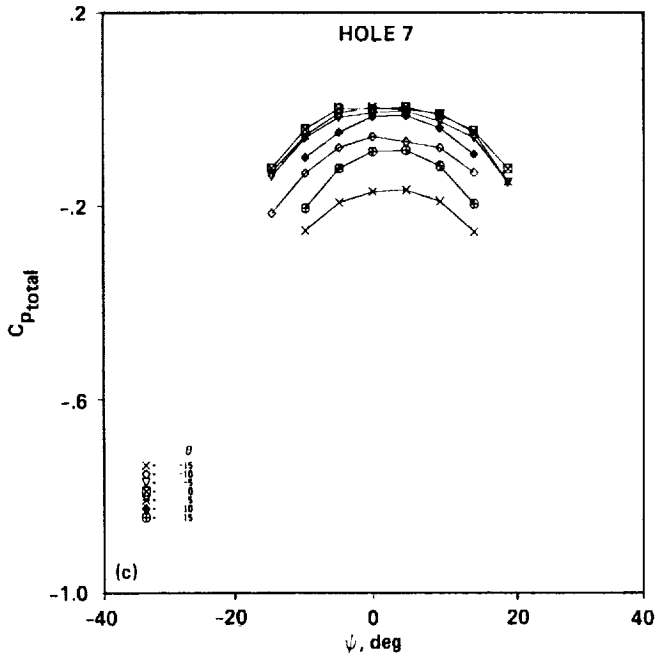

(c) Total pressure coefficients for hole 7 (low flow angle).

Figure 10.– Continued.

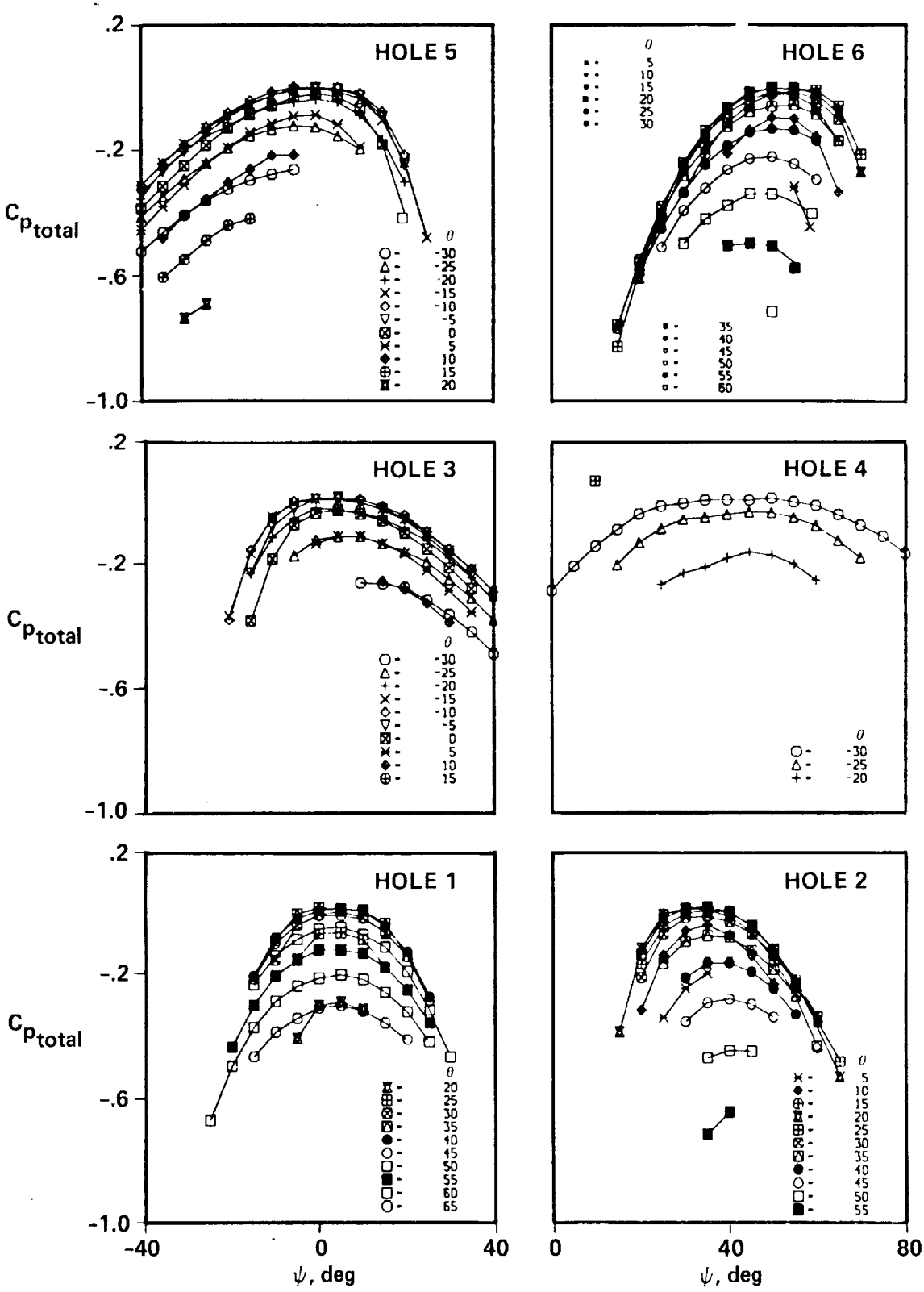

(d) Total pressure coefficients for holes 1 to 6 (high flow angle).

Figure 10.– Continued.

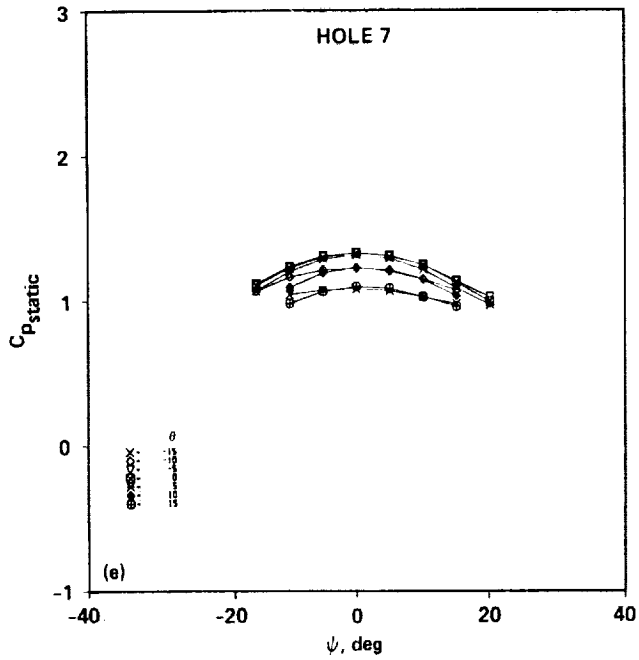

(e) Static pressure coefficients for hole 7 (low flow angle).

Figure 10.– Continued.

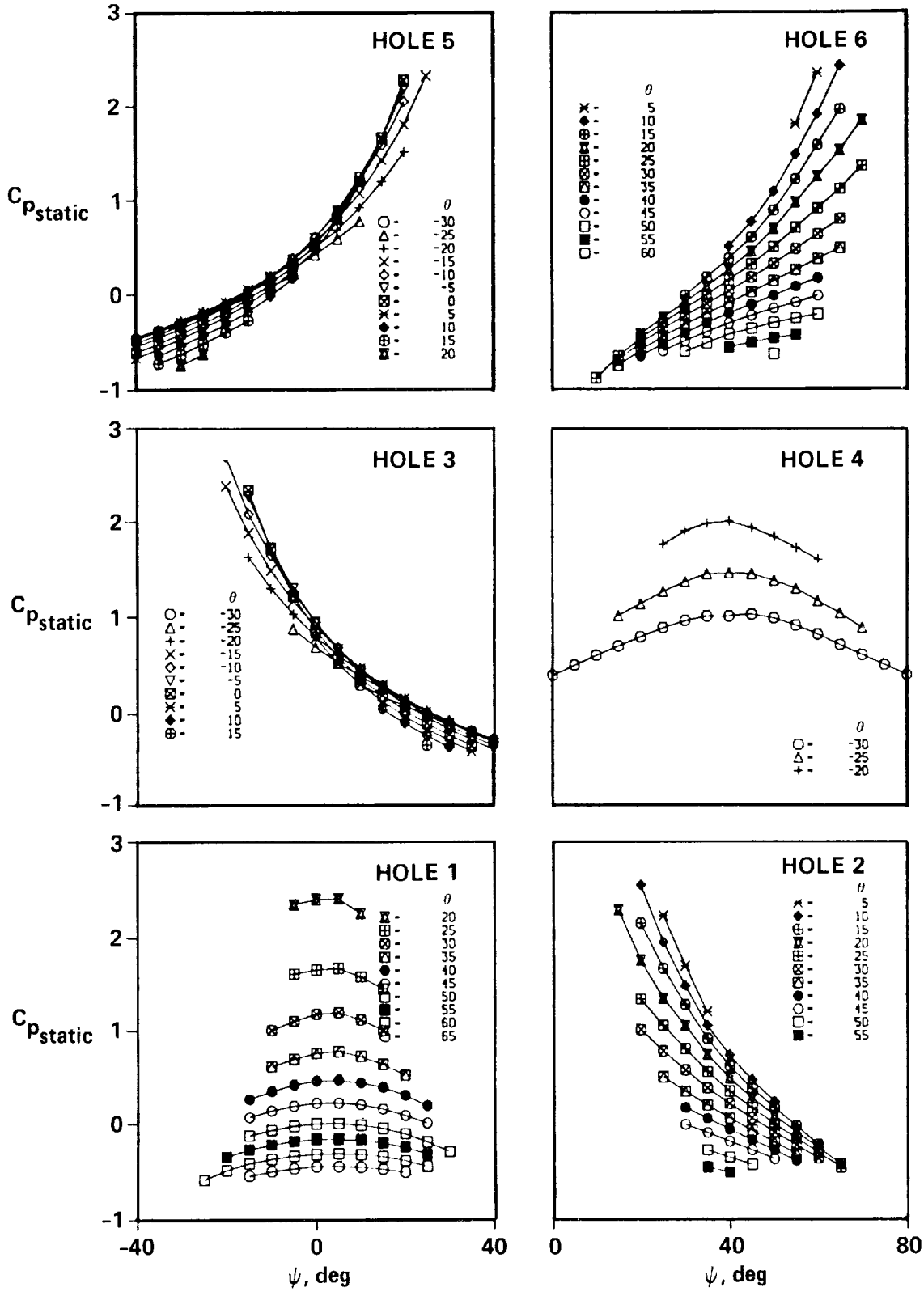

(f) Static pressure coefficients for holes 1 to 6 (high flow angle).

Figure 10.– Concluded.

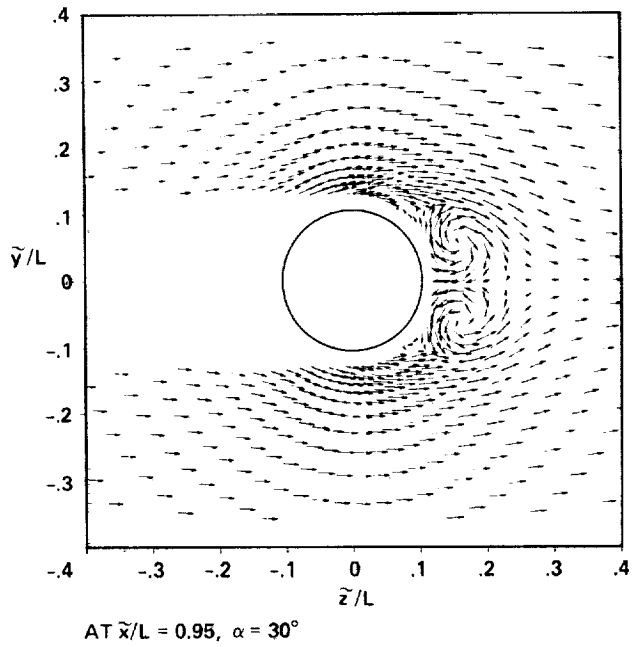

Figure 11.– Ogive-cylinder crossflow velocity vectors, Re_L = 820,000, $\alpha = 30°$.

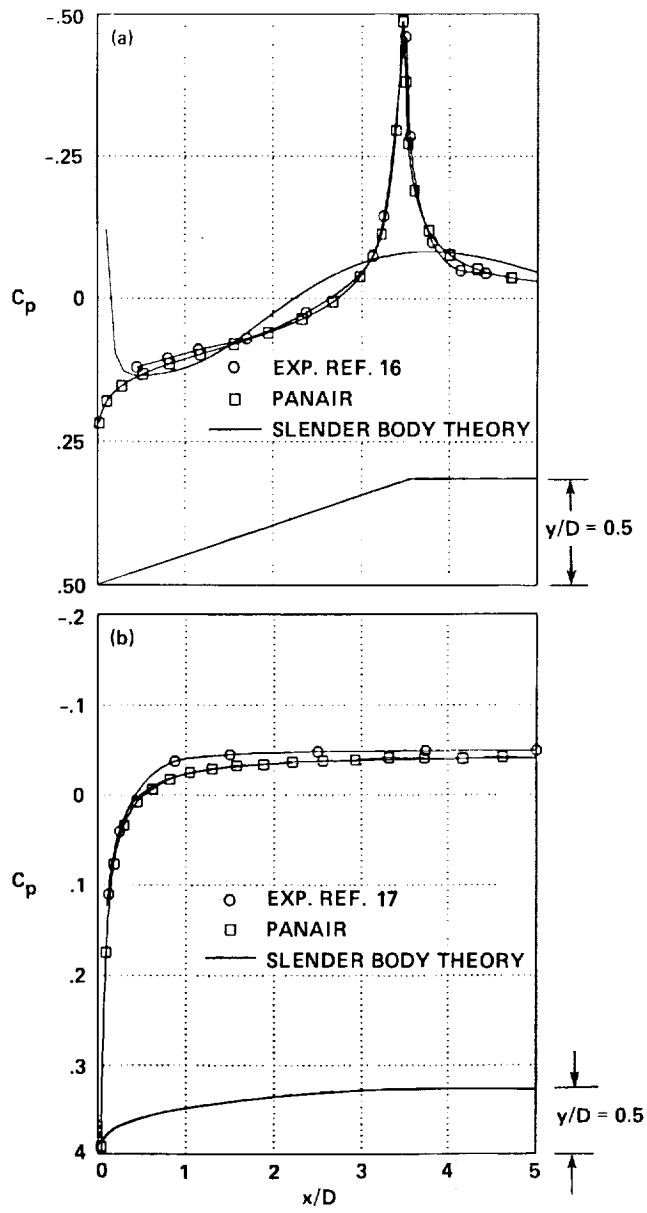

Figure 12.– Surface pressure distribution at $\alpha = 0°$. (a) Cone cylinder; (b) prolate spheroid.

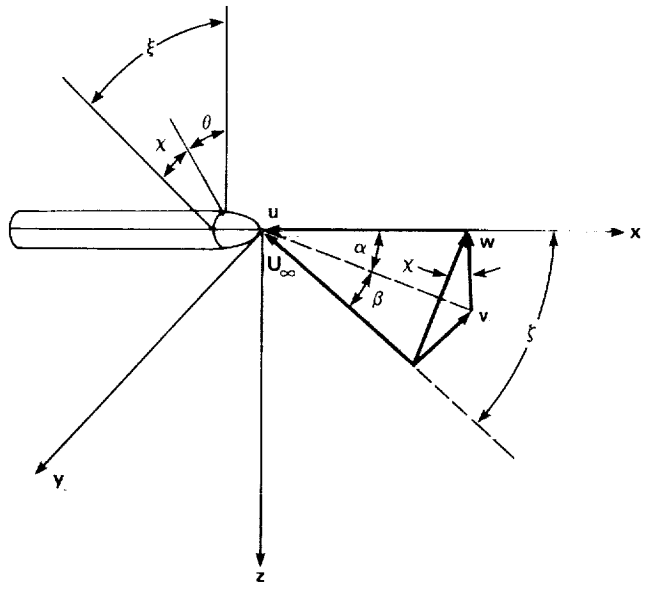

Figure 13.– Probe flow angles and coordinate system.

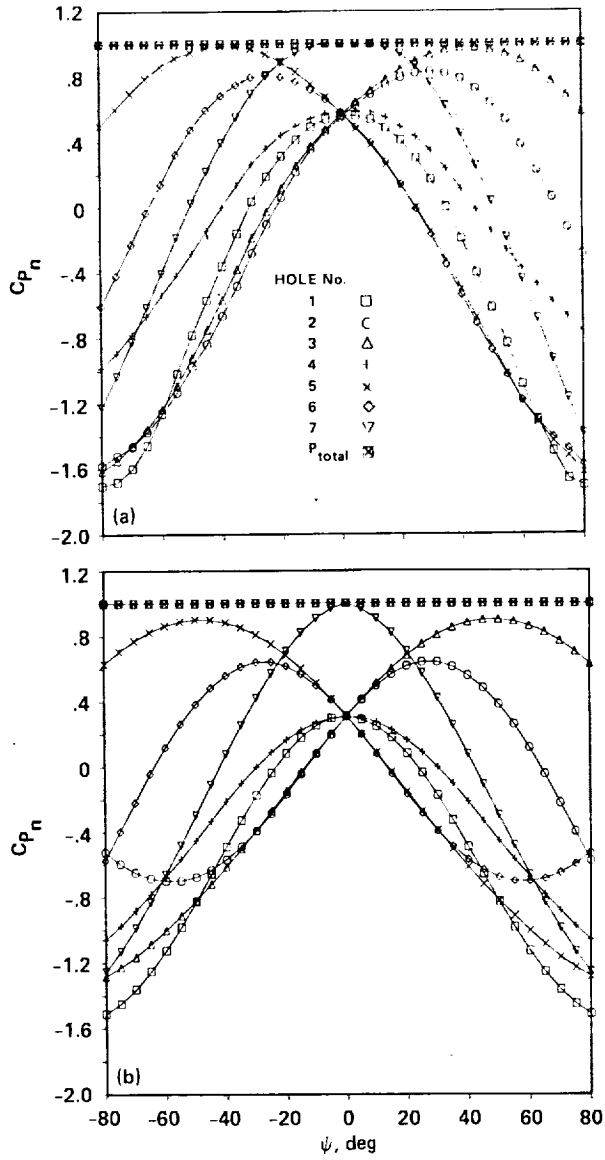

Figure 14.– Seven-hole pressure variation at $\theta = 0°$. (a) Measured pressure variation; (b) theoretical pressure variation.

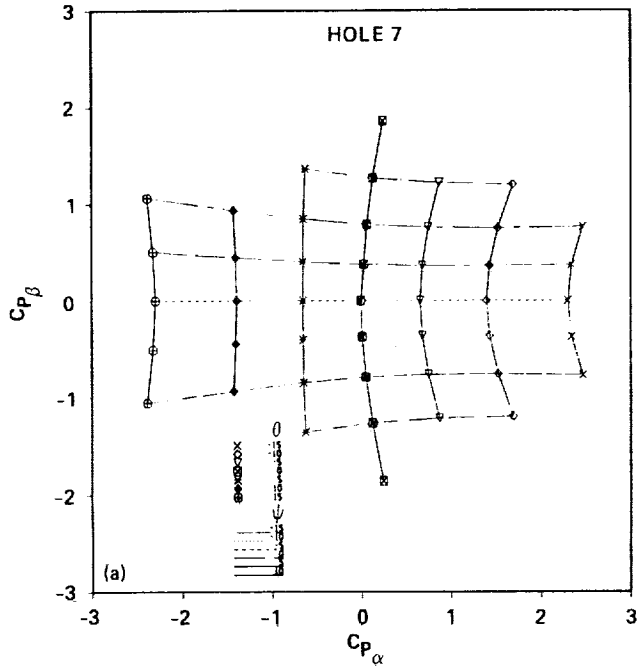

(a) Direction coefficients for hole 7 (low flow angle).

Figure 15.– Theoretical flow direction coefficients for a seven-hole probe (low flow angle).

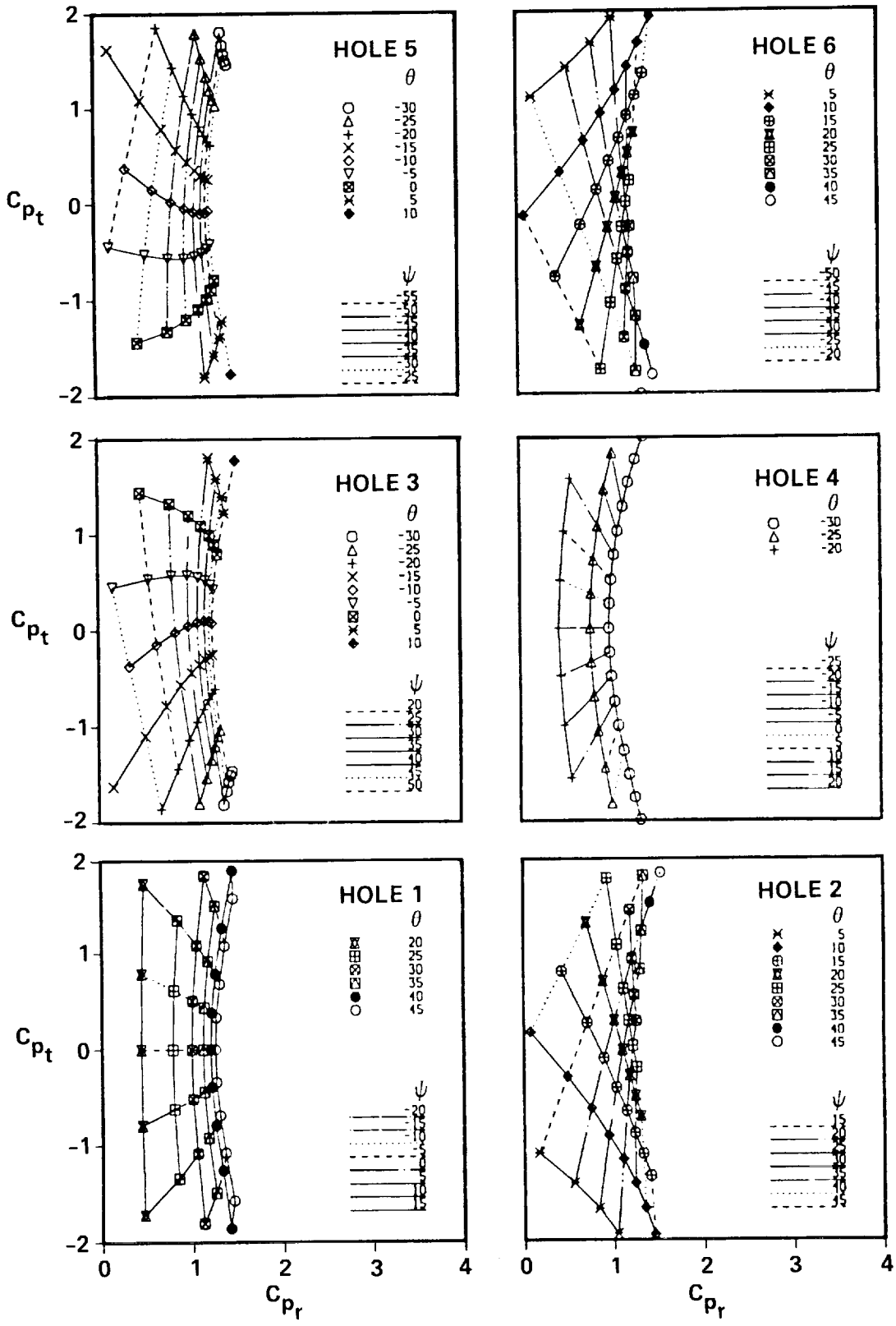

(b) Direction coefficients for holes 1 to 6 (high flow angle).

Figure 15.– Continued.

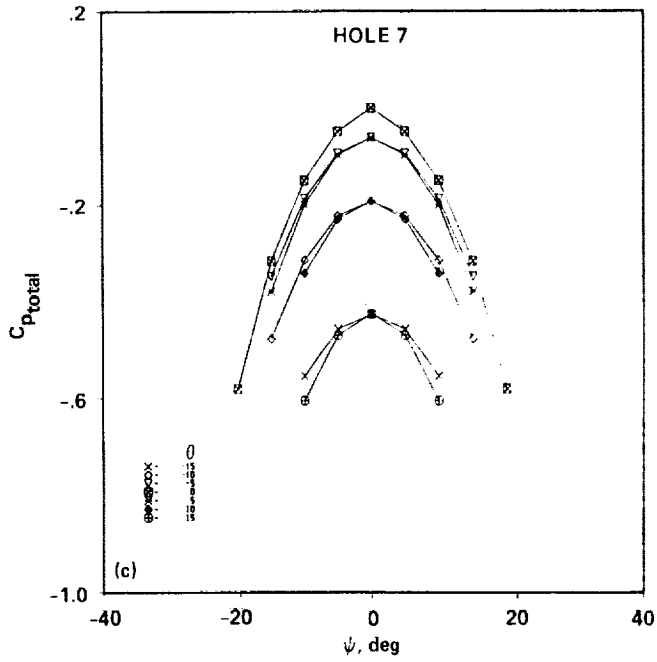

(c) Total pressure coefficients for hole 7 (low flow angle).

Figure 15.– Continued.

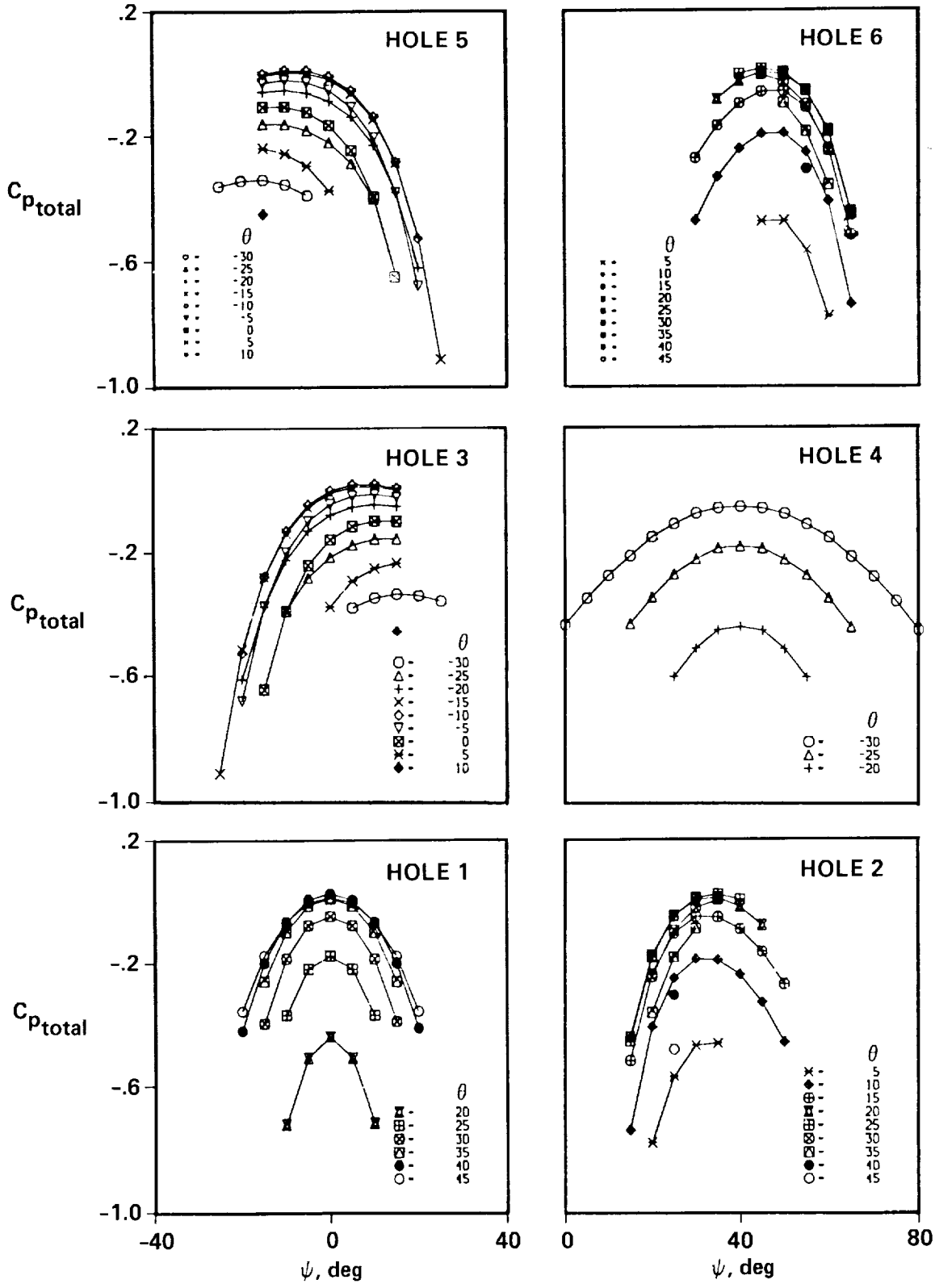

(d) Total pressure coefficients for holes 1 to 6 (high flow angle).

Figure 15.– Continued.

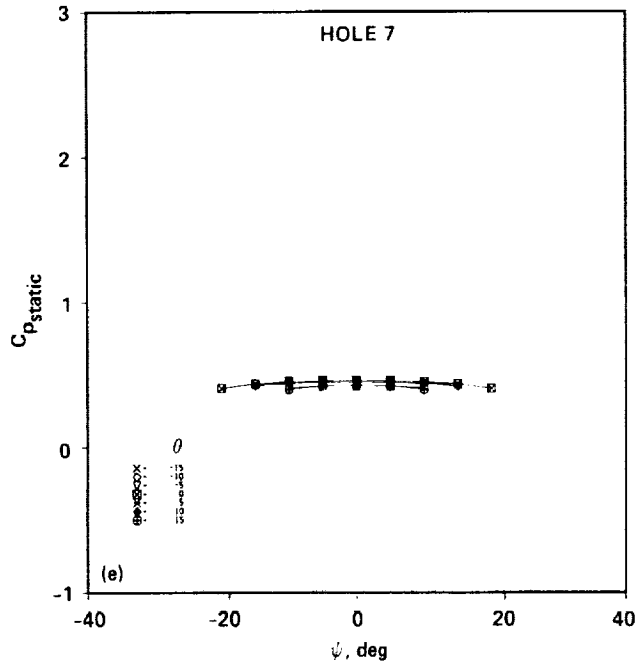

(e) Static pressure coefficients for hole 7 (low flow angle).

Figure 15.– Continued.

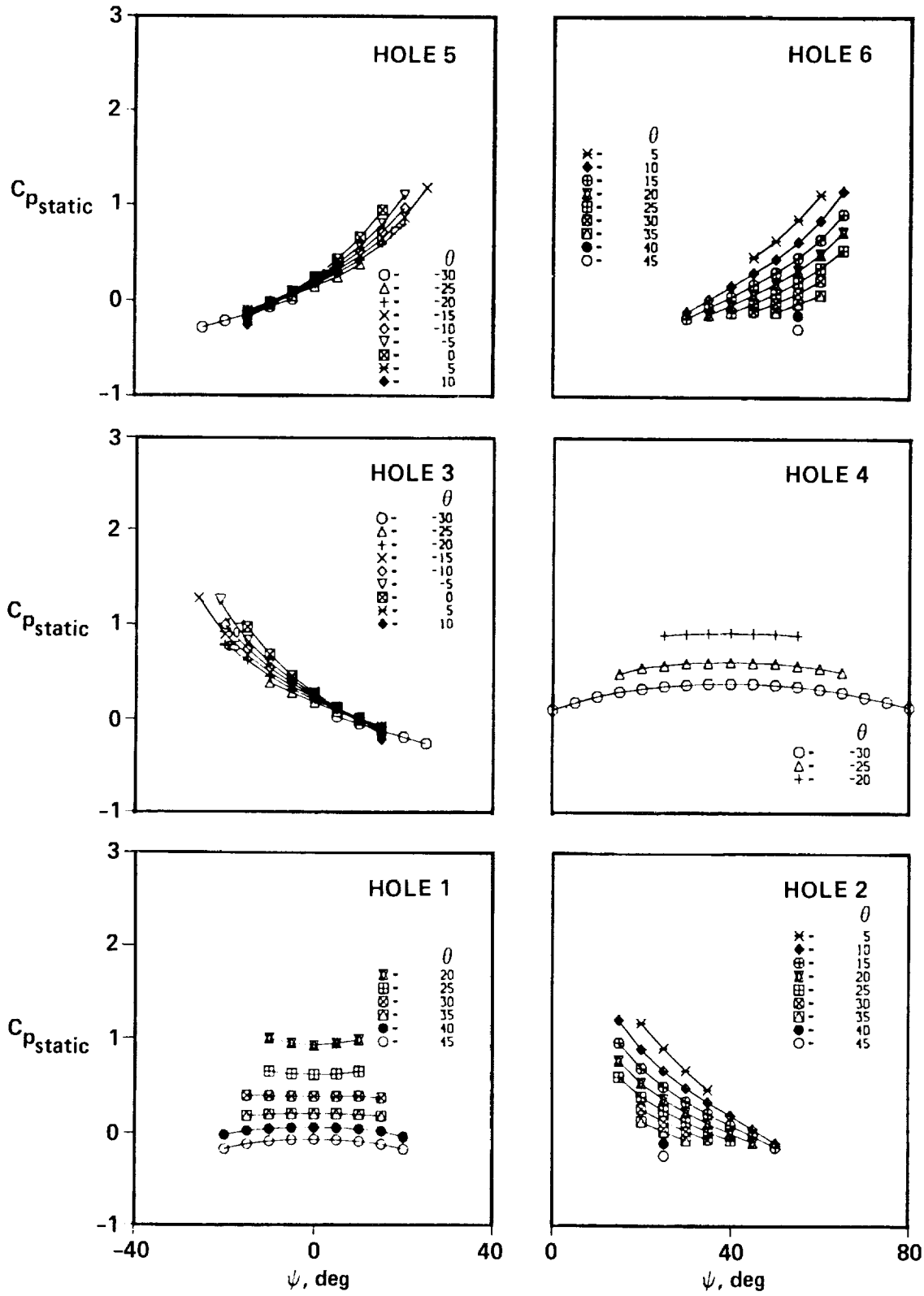

(f) Static pressure coefficients for holes 1 to 6 (high flow angle).

Figure 15.– Concluded.

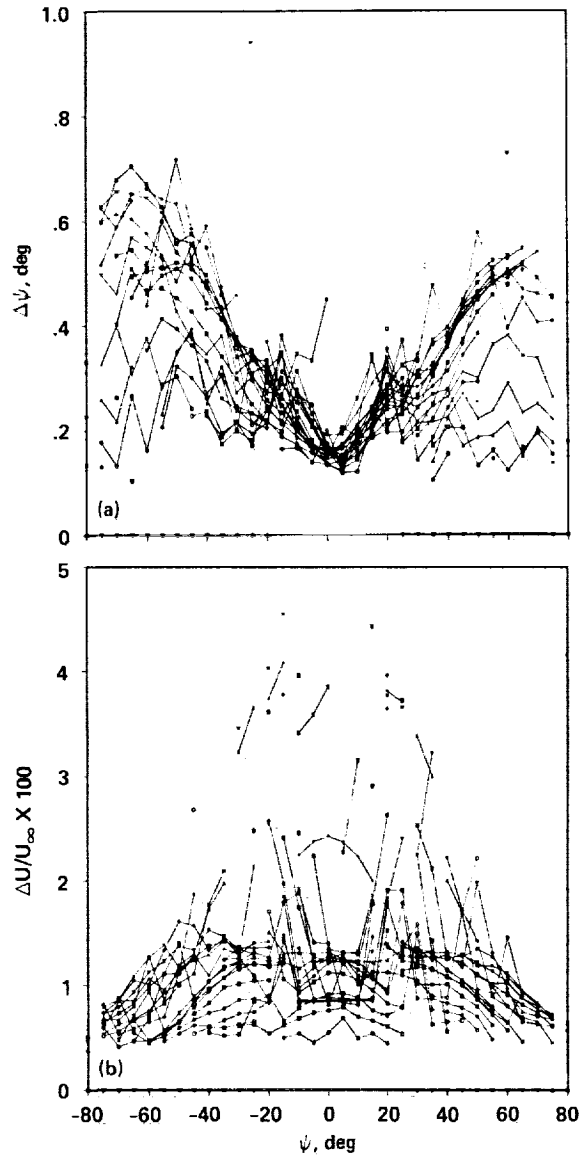

Figure 16.– Seven-hole probe measurement error. (a) Flow angle error; (b) velocity magnitude error.